

Encapsulation of Phosphorescent Pt(II) Complexes in Zn-Based Metal–Organic Frameworks toward Oxygen-Sensing Porous Materials

Tim-Oliver Knedel,[#] Stefan Buss,[#] Iván Maisuls, Constantin G. Daniliuc, Carsten Schlüsener, Philipp Brandt, Oliver Weingart, Annette Vollrath, Christoph Janiak,* and Cristian A. Strassert*

Cite This: *Inorg. Chem.* 2020, 59, 7252–7264

Read Online

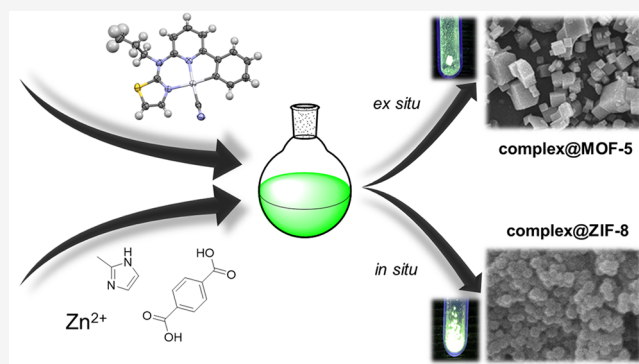
ACCESS |

Metrics & More

Article Recommendations

Supporting Information

ABSTRACT: In this work, we synthesized two tailored phosphorescent Pt(II) complexes bearing a cyclometalating tridentate thiazole-based C[^]N[^]N pincer luminophore (L) and exchangeable chlorido ([PtCl(L)]) or cyanido ([PtCN(L)]) coligands. While both complexes showed photoluminescence from metal-perturbed ligand-centered triplet states (³MP-LC), [PtCN(L)] reached the highest phosphorescence quantum yields and displayed a significant sensitivity toward quenching by ³O₂. We encapsulated them into two Zn-based metal–organic frameworks, namely, MOF-5 and ZIF-8. The incorporation of the organometallic compounds in the resulting composites [PtCl(L)]@ZIF-8, [PtCN(L)]@ZIF-8, [PtCl(L)]@MOF-5, and [PtCN(L)]@MOF-5 was verified by powder X-ray diffractometry, scanning electron microscopy, time-resolved photoluminescence spectroscopy and microscopy, as well as N₂- and Ar-gas sorption studies. The amount of encapsulated complex was determined by graphite furnace atomic absorption spectroscopy, showing a maximum loading of 3.7 wt %. If compared with their solid state forms, the solid-solution composites showed prolonged ³O₂-sensitive excited state lifetimes for the complexes at room temperature, reaching up to 18.4 μs under an Ar atmosphere, which is comparable with the behavior of the complex in liquid solutions or even frozen glassy matrices at 77 K.



INTRODUCTION

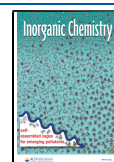
Platinum(II)-based luminescent coordination compounds featuring a d⁸ electronic configuration have been in the focus of research efforts due to their excited state properties and the applications derived from their phosphorescence.^{1–11} Inter-system crossing into the triplet manifold and radiative relaxation from the lowest triplet state is facilitated by the significant spin–orbit coupling associated with the participation of late transition elements in the electronic excited states, which constitutes a largely relativistic metal-based perturbation. The research fields span from catalysis,^{1,2} bioimaging,^{3–5} and biomedical applications^{6,7} to uses in organic light emitting devices (OLEDs).^{8–11}

Due to their strong sigma-donating effect, cyclometalating luminophores greatly improve the photophysical properties (prolonged excited state lifetimes τ and increased photoluminescence quantum yields Φ_L) by enhancing the ligand field splitting between occupied and empty d orbitals. Thus, the activation barrier for the thermal occupation of dissociative metal-centered excited states is enhanced, which in turn diminishes the population of electronic states that otherwise lead to radiationless relaxation favored by conical intersections with the ground state.¹¹ In this sense, significant advancements

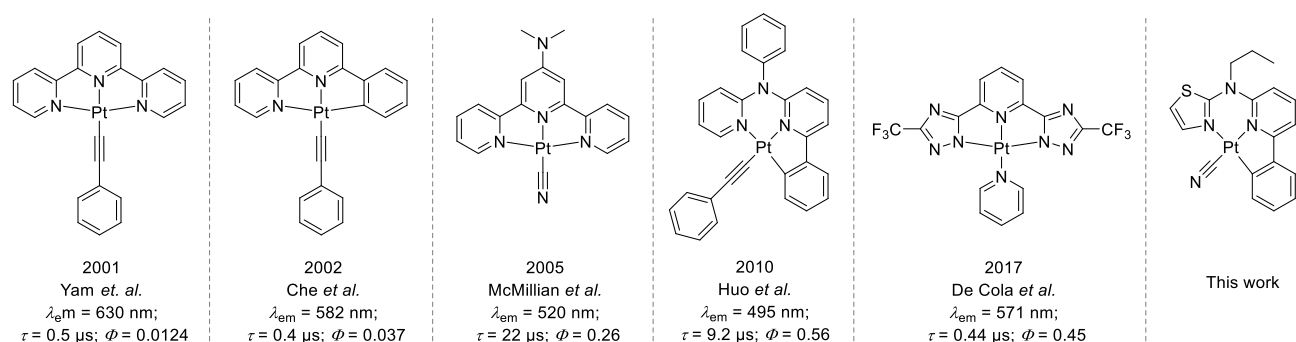
have been made in the design of improved coordination compounds.^{12,13} Huo and co-workers showed that the change from a five–five-membered metallacycle system C[^]N[^]N to a six–five-membered metallacycle C[^]N[^]N system leads to higher Φ_L due to better coordination geometries and orbital overlap.¹⁴ These effects are further enhanced by removal of π -donating ancillary ligands and insertion of strong π acceptors, e.g., exchange of chlorido by cyanido units. For luminescent metal complexes with tridentate luminophoric ligands, the coligand can influence the solubility, and also the tendency toward aggregation can be modulated.^{15,10} The ancillary ligand can also facilitate the covalent embedment into supramolecular assemblies for biomedical applications, as we have recently reported in collaboration with Gianneschi and co-workers regarding the use of a norbornene-substituted pyridine leading

Received: March 4, 2020

Published: May 7, 2020



Scheme 1. Previously Described Pt(II) Complexes Bearing Tridentate Luminophores and Comparison with the Herein Reported Design Pattern^{11,14,15,52,53}



to biocompatible micelles for multimodal bioimaging with dual orthogonal readouts.¹⁶

The excited state properties are significantly affected by the environment, including solvents, aggregation state (e.g., amorphous solids vs crystals or solutions),^{17,18} frozen glassy matrices vs polymers, as well as the presence of ³O₂^{19,20} and other dynamic or static quenchers.^{21,22} Among others, the differences in dielectric constants of solvents can lead to a shift in the emission maxima (solvatochromic effect) and in the charge-transfer character of the emissive excited triplet states where an enhanced participation of the metal center increases the radiative rate constant by favoring spin–orbit coupling and mixing of states with different spin multiplicities. If the emitter is restricted from vibronic relaxation at low temperatures or in confined (or rigid) environments, the radiative relaxation is relatively favored. Intermolecular interactions can differ depending on aggregation at higher concentrations, in condensed phases, or in glassy matrices. In liquid solution, aggregation can be controlled by varying the concentration and the bulk of the coligand. In addition, the strategy of a “solid-solution” environment²³ can be used, as recently reported by Che and co-workers for a Pt(II) complex embedded in a metal–organic framework (MOF).²⁴ In his work, the MOFs were used as concentrators for the Pt(II) complexes to induce aggregation inside them and leading to ³MMLCT emission.²⁴ Otherwise and to the best of our knowledge, the behavior of monomeric Pt(II)-based triplet emitters in MOFs has been rarely explored,²⁵ despite their potential uses as (photo)-catalysts or sensors.²⁴

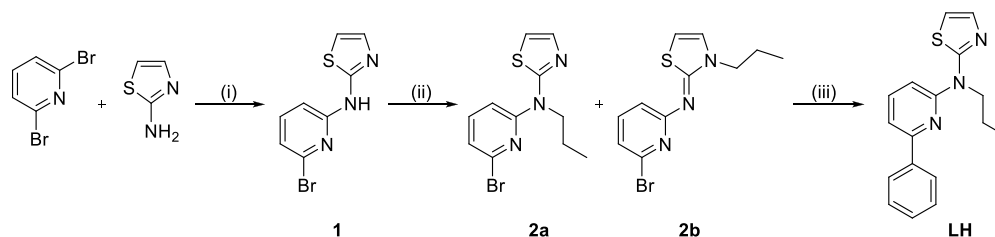
MOFs are suitable scaffolds for the encapsulation of various molecular species including metal complexes, nanoparticles, dyes, or enzymes.^{26–30} Their defined pore structure and variable linkers make MOFs tunable for various applications including catalysis,^{31–33} drug delivery,³⁴ or molecular sensing.^{35,36} Porous luminescent MOFs including the encapsulation of photofunctional complexes play an important role in photocatalysis or as sensors for quenching species such as ³O₂.^{37,38} For example, Xu and co-workers as well as Matsuoka and co-workers both functionalized a metal–organic framework (MOF-253 and Zr-MOF-bpy, respectively) with PtCl₂ to form a Pt(II) complexes where the MOF-linker acted as a ligand for potential applications in photocatalytic hydrogen production.^{39,40} By modification of the linker, Shi and co-workers bound a Ru(II) complex to the MOF scaffold, producing a composite that is suitable for photocatalysis.⁴¹ Another postsynthetic approach was used by Gao and co-workers to encapsulate an Ir(III) complex into UiO-66, which

is also relevant for photocatalysis.⁴² Metal complex incorporation into MOFs is generally carried out by postsynthetic encapsulation with or without linker modification. Although the *in situ* encapsulation of small molecules has been previously described,^{43–45} the *in situ* immobilization of metal ligand coordination compounds into a MOF has been rarely explored,²⁴ despite being a common strategy for enzymes.^{46–51}

In this work, we synthesized and encapsulated two photoluminescent Pt(II) complexes with long excited state lifetimes in the well-established Zn(II)-based scaffolds MOF-5⁵⁴ and ZIF-8⁵⁵ while exploring an *in situ* and *ex situ* approach in order to investigate the behavior of the entrapped d⁸-configured triplet emitters. The tridentate ligand precursor *N*-(2-phenylpyridine)-*N*-propyl-thiazole-2-amine (Scheme 1) was designed to provide a mostly planar coordination plane and a side-group favoring processability in organic solvents without major steric constraints. A cyanido coligand provided an enhanced ligand-field splitting with nearly no additional steric demand. The metal complexes were fully characterized, including time-resolved photoluminescence spectroscopy, whereas the encapsulated amount of complex inside MOFs was determined by graphite furnace atomic absorption spectroscopy. The resulting composites were analyzed by X-ray diffractometry, electron microscopy, N₂- and Ar-sorption measurements, time-resolved photoluminescence spectroscopy, and microscopy.

RESULTS AND DISCUSSION

We designed and realized a new thiazole-based C[∧]N*N-type luminophore as a suitable pincer ligand precursor (LH) in a three-step synthetic procedure, paying attention to a minimized bulk to favor encapsulation in a MOF matrix while providing a strong ligand field splitting owing to cyclometalation and a close-to-ideal coordination geometry. Hence, we obtained the corresponding Pt(II) chlorido complex [PtCl(L)] via an ortho-directed cyclometalation, as well as the corresponding cyanido coordination compound [PtCN(L)] upon exchange of the coligand, thus maximizing the thermal activation barrier toward metal-centered dissociative states that might potentially quench the emissive triplet state. Each new intermediate and complex was characterized by one- and two-dimensional nuclear magnetic resonance (NMR, Figures S1–S30) spectroscopy as well as mass spectrometry (EM-ESI-MS). The metal complexes were further analyzed by infrared (IR; Figures S31–S32), single crystal X-ray diffractometry, and time-resolved photoluminescence spectroscopy. Subsequently, the Pt(II) complexes were

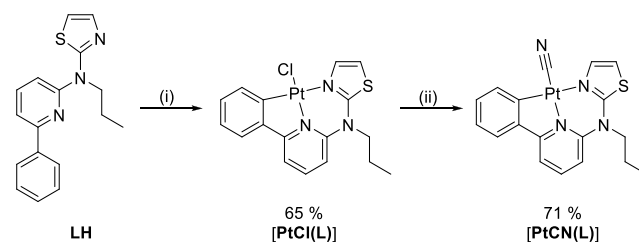
Scheme 2. Three-Step-Synthesis of the Ligand Precursor LH^a

^a(i) Buchwald-Hartwig cross-coupling: Na₂CO₃, Xantphos, Pd₂(dba)₃, toluene, ^tBuOH, H₂O, 130 °C, 72 h, 49% yield. (ii) Alkylation: 1-bromopropane, Cs₂CO₃, THF, 80 °C, 16 h, 40% yield for **2a**, 51% yield for **2b**. (iii) Suzuki cross-coupling: phenylboronic acid, K₂CO₃, Pd(PPh₃)₄, THF, H₂O, 80 °C, 16 h, 83% yield.

embedded in the MOFs ZIF-8 and MOF-5 by *in situ* encapsulation or postsynthetic incorporation, respectively. The obtained complex@MOF composites were analyzed by powder X-ray diffractometry (PXRD), N₂ sorption, Ar sorption, graphite furnace and flame atomic absorption spectroscopy (GFAAS and FAAS), and scanning electron microscopy (SEM). Time-resolved photoluminescence spectroscopy measurements were carried out in the air and under Ar. The detailed procedures and additional structural and spectroscopic data can be found in the Supporting Information (SI).

Synthesis of [PtCl(L)] and [PtCN(L)]. The intermediate compound **1** (Scheme 2) was obtained by a Buchwald-Hartwig-cross coupling reaction. As expected, alkylation of **1** yielded two possible products, due to the tautomeric behavior of amino-thiazoles leading to the exo- (**2a**) as well as to the endocyclic (**2b**) products. Mihovilovic and co-workers previously investigated the substitution reaction of amino-thiazoles for a synthetic purpose.⁵⁶ Using their optimized conditions (DMF, NaH, room temperature) to obtain the amine derivative⁵⁷ led in our case to a product ratio of 1:1.8 (**2a/2b**). Switching to Cs₂CO₃ in refluxing THF overnight resulted in a slightly better ratio of 1:1.3 with a yield enhancement from roughly 30% to nearly 40% for **2a**. The ³J_{HH}-coupling constant of the thiazole gives a good indication for the substitution pattern as previously reported in the literature.^{56,57} For the amine derivatives (**2a**), these values are found around ³J_{HH} = 3.6 Hz, whereas the imine (**2b**) shifts to ³J_{HH} = 4.8 Hz. The last step toward the ligand precursor LH was realized by means of a Suzuki-cross-coupling reaction. After obtaining the ligand precursor LH, the Pt(II) complex was obtained using cyclometalation reaction conditions (K₂[PtCl₄], ⁿBu₄NCl, AcOH, 130 °C) to yield the chlorido complex [PtCl(L)]. As previously observed upon alkylation on the thiazole ring, coordination of the metal center shifts the coupling constants to roughly ³J_{HH} = 4.0 Hz. The ancillary ligand exchange was carried out using AgCN, yielding the corresponding cyanido complex [PtCN(L)]. The herein described synthetic route is summarized in Schemes 2 and 3.

Molecular Structures in Single Crystals As Obtained by X-Ray Diffractometry. For **1**, **2b**, [PtCl(L)], and [PtCN(L)], the structural data are given in the SI (Tables S1–S4; Figures S33–S36). The crystal structures of [PtCl(L)] and [PtCN(L)] are isomorphous to each other with the trigonal space group of R $\bar{3}$. Pt(II) shows the expected square coordination geometry in an almost planar environment (compare Figures 1 and S35). The largest deviation from the perfect quadratic coordination around the Pt(II) centers

Scheme 3. Cyclometalation and Ligand Exchange Towards the Desired Pt(II) Complexes^a

^a(i) K₂[PtCl₄], ⁿBu₄NCl, glacial acetic acid, 130 °C, 16 h, 65% yield; (ii) AgCN, MeCN, CHCl₃, 80 °C, 71% yield.

involves the angle encompassing the five-membered metallacycle. For [PtCN(L)], this angle corresponds to 82.25° (N3–Pt1–C31), while the overall angle sum adds up to 359.50°. In general, the characteristic values for these C^N*N-type complexes agree with the literature for comparable compounds.¹⁴ The main intermolecular interaction in both complexes can be described as π – π ⁵⁸ and CH– π interactions (Tables S3 and S4).⁵⁹ A special feature is the dimer formation involving two molecular units. For [PtCl(L)] and [PtCN(L)], the nearest centroid–centroid distances (3.400 and 3.440 Å, respectively) suggest a dimer interaction between two adjacent molecules (Figure 1 right, Figures S35B and S36B), while the relatively long Pt–Pt distances (5.905 Å for [PtCl(L)] and 5.860 Å for [PtCN(L)]) indicate that this interaction is purely π – π in nature.⁵⁸ Slightly extended but more strongly slipped π – π interactions between the dimeric pairs lead to the formation of linear chains (Figures S35 C and S36 C).

Time-Resolved Photoluminescence Spectroscopy of [PtCl(L)] and [PtCN(L)]. Figure 2 shows the absorption and photoluminescence spectra of [PtCl(L)] and [PtCN(L)]; their photophysical properties are summarized in Table 1 (the complete set of spectra, photoluminescence decay plots, and photoluminescence micrographs are shown in Figures S37–S57). The maxima in the UV/vis-absorption spectra (Figure 2A) show the typical vibrational progressions that can be assigned by comparison with related compounds.^{14,18} The bands at short wavelengths associated with high molar absorption coefficients can be attributed to a transitions into excited singlet states possessing ligand-centered character (¹LC/¹ $\pi\pi^*$). The bands at lower energies (325–425 nm) can be described as transitions into singlet excited states with mixed ligand-centered and metal-to-ligand charge-transfer character (¹LC and ¹MLCT, respectively). The absorption band at 395 nm for [PtCN(L)] can be assigned to a transition

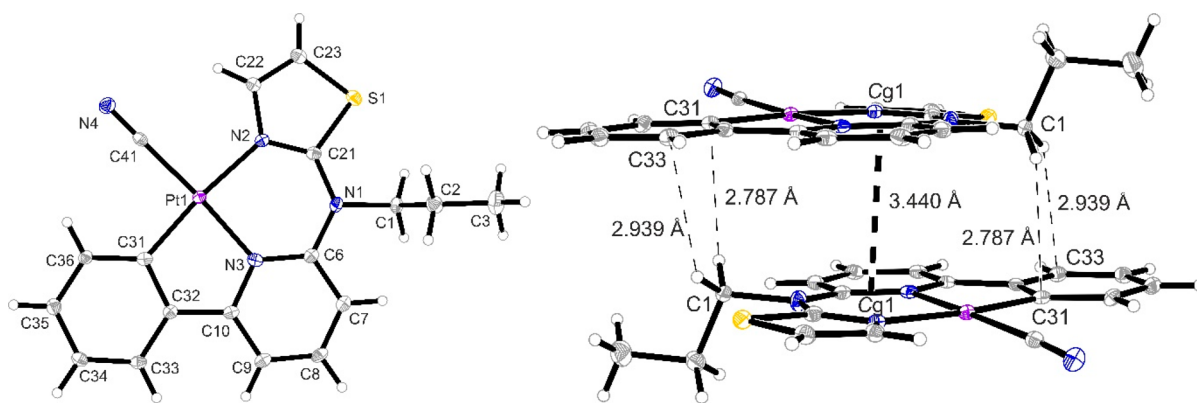


Figure 1. Molecular structure of $[\text{PtCN}(\text{L})]$ (left) as obtained by X-ray diffractometry on a single crystal. Dimer type formation involving $\pi\cdots\pi$ and $\text{C}-\text{H}\cdots\pi$ interactions (right). Thermal ellipsoids are shown at 30% probability.

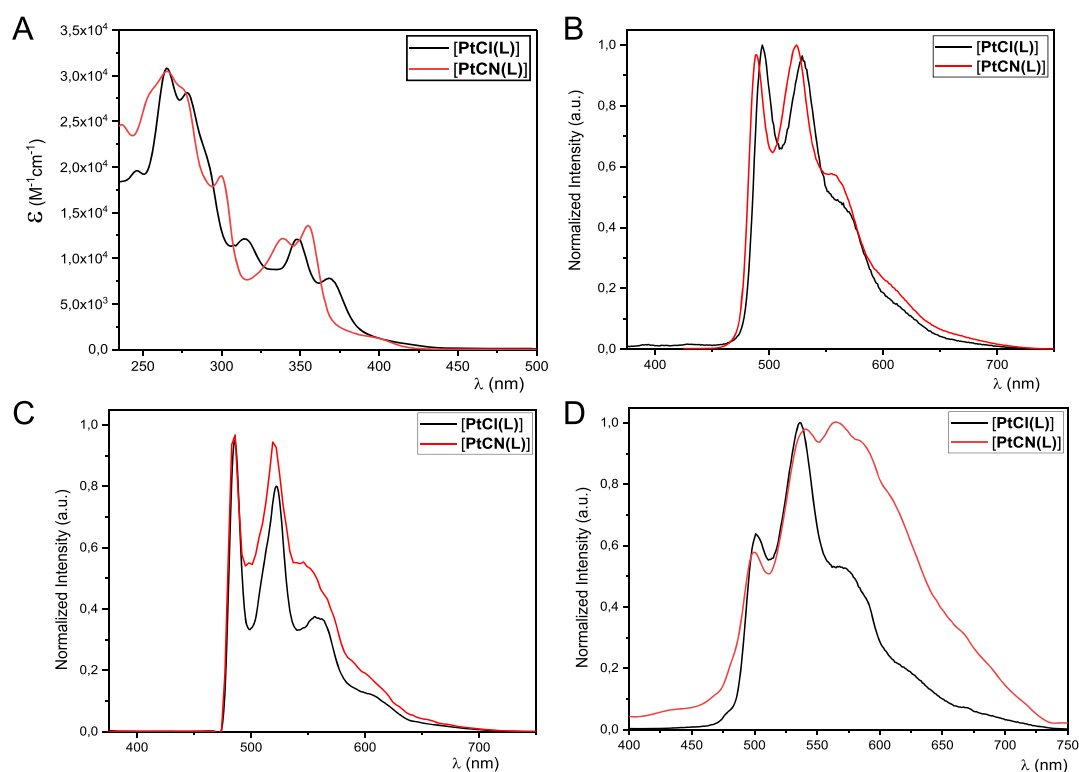


Figure 2. (A) UV/vis-absorption spectra of $[\text{PtCl}(\text{L})]$ (black) and $[\text{PtCN}(\text{L})]$ (red) in DCM at 298 K; (B) photoluminescence spectra ($\lambda_{\text{exc}} = 350$ nm) of $[\text{PtCl}(\text{L})]$ (black) and $[\text{PtCN}(\text{L})]$ (red) in fluid DCM at 298 K; (C) photoluminescence spectra ($\lambda_{\text{exc}} = 350$ nm) of $[\text{PtCl}(\text{L})]$ (black) and $[\text{PtCN}(\text{L})]$ (red) in a frozen glassy matrix (DCM/MeOH 1:1) at 77 K; (D) photoluminescence spectra ($\lambda_{\text{exc}} = 350$ nm) of $[\text{PtCl}(\text{L})]$ (black) and $[\text{PtCN}(\text{L})]$ (red) as neat solids.

into a mainly pure $^1\text{MLCT}$ state, due to the correspondingly low molar absorption coefficient ($1.5 \times 10^3 \text{ M}^{-1} \text{ cm}^{-1}$).

The excitation spectra of both complexes resemble the absorption spectra. The emission spectra (Figures 2B and C) show the typical vibrational progressions associated with the emission from MP-LC states. The differences between the spectra of the chlorido and cyanido complexes in fluid solution and frozen glassy matrices are marginal, which shows that the coligand only has a very small influence on the energy of the emissive excited states. The excited state properties are mainly dominated by the tridentate luminophore **L** with a perturbation from the Pt(II) center. On the other hand, the coligand change has a significant impact on Φ_{L} and τ . Overall, the radiative process is relatively more efficient for the cyanido

complex $[\text{PtCN}(\text{L})]$, due to the enhanced ligand field-splitting that suppresses radiationless deactivation pathways, thus prolonging τ and enhancing Φ_{L} . The τ in solution for $[\text{PtCl}(\text{L})]$ is rather short (17.50 ns) and thus insensitive to diffusional quenching by dissolved $^3\text{O}_2$, which is also true for the rather low Φ_{L} (<0.02). On the other hand, the cyanido complex $[\text{PtCN}(\text{L})]$ displays a $\tau = 0.69 \mu\text{s}$ and a low Φ_{L} (<0.02) that both rise drastically upon deaeration to reach values of $\tau = 33.5 \mu\text{s}$ and $\Phi_{\text{L}} = 0.46$. In frozen glassy matrices at 77 K, both compounds show even longer τ values ($31.2 \mu\text{s}$ for $[\text{PtCl}(\text{L})]$ and $42.3 \mu\text{s}$ for $[\text{PtCN}(\text{L})]$) and nearly unitary Φ_{L} .

In solid phases, the behavior differs quite strongly from the solutions and glassy matrices. The powder of $[\text{PtCl}(\text{L})]$ shows a different vibrational progression where the second maximum

Table 1. Photophysical Data for the Complexes [PtCl(L)] and [PtCN(L)]

	[PtCl(L)]			[PtCN(L)]	
fluid solution (DCM, 298 K)	$\lambda_{\text{abs}}/\text{nm}$ ($\epsilon/10^3 \text{ M}^{-1}\text{cm}^{-1}$)	265 (30.8), 277 (28.0), 313 (12.0), 348 (12.1), 368 (7.8)		255 (28.2), 265 (30.5), 275 (28.7), 300 (19.0), 339 (12.2), 355 (13.6), 395 (1.5)	
	$\lambda_{\text{exc}}/\text{nm}$	352, 370		311, 360, 390 (shoulder)	
	$\lambda_{\text{em}}/\text{nm}$	494, 530, 555 (shoulder)		489, 524, 555 (shoulder)	
	$\tau/\mu\text{s}^c$	$17.50 \times 10^{-3} \pm 0.13 \times 10^{-3, a}$	$17.9 \times 10^{-3} \pm 0.7 \times 10^{-3}$ [$24 \times 10^{-3} \pm 2 \times 10^{-3}$ (6); $17.50 \times 10^{-3} \pm 0.18 \times 10^{-3}$ (94)] ^b	0.686 ± 0.005^a	33.5 ± 0.2^b
	$\Phi \pm 0.02$	$<0.02^a$	$<0.02^b$	$<0.02^a$	0.46^b
frozen glassy matrix (DCM/MeOH 1:1, 77 K)	$\lambda_{\text{exc}}/\text{nm}$	318, 348, 367		310, 371, 400 (shoulder)	
	$\lambda_{\text{em}}/\text{nm}$	484, 522, 556		486, 522, 549 (shoulder)	
	$\tau/\mu\text{s}^c$	31.2 ± 1.0 [38.9 ± 0.5 (40); 26.0 ± 0.4 (60)]		42 ± 2 [65.8 ± 0.9 (37); 33.7 ± 0.9 (51); 8 ± 3 (13)]	
	$\Phi \pm 0.02$	0.98		0.98	
powders (298 K)	$\lambda_{\text{em}}/\text{nm}$	501, 536, 570 (shoulder)		501, 545, 566	
	$\tau/\mu\text{s}^c$	0.75 ± 0.04 [1.47 ± 0.05 (28); 0.627 ± 0.014 (72)] ^a	0.79 ± 0.04 [1.44 ± 0.04 (18); 0.652 ± 0.013 (82)] ^b	1.30 ± 0.17 [8.7 ± 0.4 (4); 2.21 ± 0.13 (21); 0.63 ± 0.04 (75)] ^a	2.0 ± 0.3 [12.0 ± 0.7 (5); 3.6 ± 0.2 (24); 0.82 ± 0.07 (71)] ^b
	$\Phi \pm 0.02$	0.04^a		0.02^a	0.02^b
crystals (298 K)	$\lambda_{\text{em}}/\text{nm}$	560, 610		525 (shoulder), 560	
	$\tau/\mu\text{s}^c$	1.44 ± 0.14 [4.8 ± 0.1 (38); 1.26 ± 0.04 (53); 0.18 ± 0.08 (10)] ^a		2.04 ± 0.14 [5.6 ± 0.4 (22); 1.45 ± 0.12 (43); 0.40 ± 0.04 (35)] ^a	

^aAerated sample. ^bDeaerated sample. ^cPhotoluminescence decays measured detecting at 530 nm. For multiexponential decays, the amplitude-weighted average lifetimes are given as well as the different components in square brackets with relative amplitudes as percentages in parentheses. $\lambda_{\text{exc}} = 350$ nm was used for the emission and Φ_{L} measurements, $\lambda_{\text{em}} = 530$ nm for excitation measurements, and $\lambda_{\text{exc}} = 376.7$ nm and $\lambda_{\text{em}} = 530$ nm were used for the lifetime measurements.

at $\lambda = 536$ nm is the most prominent band. This is due to the restriction of vibrational modes in the solid environment, but no excimeric emission band can be traced beyond 600 nm. On the other hand, the emission spectrum of [PtCN(L)] as a powder is dominated by a broad red-shifted band peaking at $\lambda = 560$ nm, which can be assigned to an excimeric state without significant intermetallic interaction. The X-ray diffractometric analysis actually showed a dimer formation with a π - π interaction of 3.440 Å, which might lead to excimers but without significant Pt-Pt interaction. The lack of excimeric emission by [PtCl(L)] in the solid state may be related to a difference in the overlap of the coordination planes and lead to a weaker influence on the emission.

Similar results were obtained if powders of the complexes or crystals thereof were investigated by using time-resolved spectroscopy or time and spectrally resolved confocal microscopy (Figures S44–S57). In any case, the solid-state photoluminescence of both complexes is not significantly influenced by $^3\text{O}_2$, which is true for Φ_{L} as well as for τ . We assume that the packing in the crystal hinders the interaction of the luminophores with $^3\text{O}_2$. In fact, we observe the formation of potential channels along the 3-fold rotation/rotoinversion axes with the alkyl chains for [PtCN(L)] and the hydrogens of the phenyl ring for [PtCl(L)] oriented into these channels (Figures S35D and S36D).

Synthesis of complex@MOF Composites. For the complex encapsulation, two Zn-based MOFs, namely, ZIF-8 and MOF-5, were selected, as their pore sizes fit the dimension of the coordination compounds (complex size roughly $8 \text{ \AA} \times 12 \text{ \AA}$, pore diameter 11 \AA for ZIF-8⁶⁰ and 13 \AA for MOF-5).⁶¹ The complex@MOF composites were prepared in two different ways (see SI for further details): The *in situ* procedure was performed for the encapsulation of the Pt(II) complexes in ZIF-8 by adding the coordination compounds to the MOF precursor and then preparing the MOF following a synthesis route described in the literature. For [PtCN(L)], the amount of complex used in the synthesis was varied to

determine the optimal amount of encapsulated complex. A post synthetic approach was not used due to the very small pore windows of ZIF-8 with only a $\sim 3 \text{ \AA}$ diameter. For the postsynthetic procedure, MOF-5 was prepared as single crystals or powder samples. The complex was then encapsulated by adding the single crystals or powders to a solution of the complex in DCM. After 24 h, the MOF samples were washed until the solution did not show any residual photoluminescence. The synthesis of MOF-5 was carried out in DMF, but since complexes are poorly soluble in this solvent, the *in situ* approach was not tried for MOF-5.

PXRD of the complex@MOF Composites. The experimental powder X-ray diffractograms of the complex@MOF composites match the simulations (Figures S58 and S59). The absence of additional reflections or reflections for [PtCN(L)] and [PtCl(L)] in the PXRDs indicates the lack of crystalline order for the embedded complex in the MOFs and rules out crystallization of the complexes at the outer MOF surface, respectively.

Sorption Measurements on the complex@MOF Composites. For porosity determination and as an indication of an encapsulated complex in the pores of the MOFs, comparative N_2 (ZIF-8 and MOF-5) and Ar gas sorption (ZIF-8) measurements were performed for neat MOFs and their composites (Figures 3 and 4 and Figures S60–S63, Table 2).

The ZIF-8 samples show an N_2 adsorption step in the relative pressure range of 0.03 to 0.05 (Figure S62). This early sorption step is known from the literature and related to a reorganization of the methylimidazolate linker, resulting in a slight pore window widening and additional gas adsorption.^{62,63} At the same time, this early adsorption step makes a BET surface area determination for this microporous material difficult (see SI, section S7, for further details). Hence, we resorted to Ar sorption for ZIF-8 and its composites, where this early step is absent (Figure 3). Also, Ar sorption is advocated for BET surface area determination of microporous

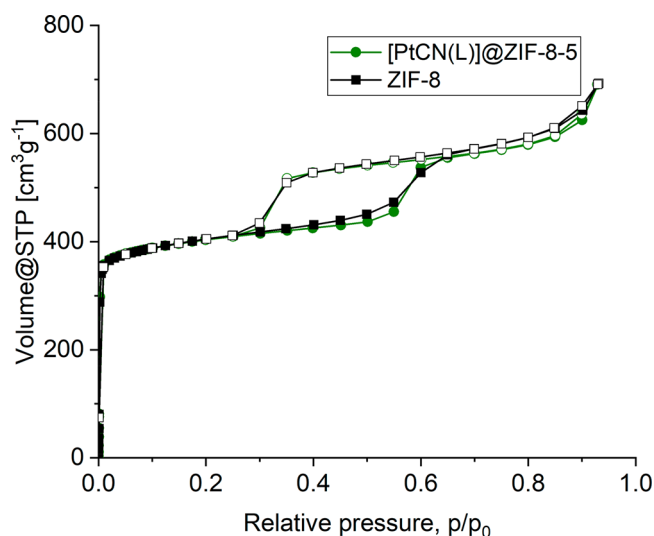


Figure 3. Ar sorption isotherms of [PtCN(L)]@ZIF-8-5 (green circles; “5” indicates the amount of Pt complex used in the composite synthesis) and neat ZIF-8 (black squares). Filled symbols, adsorption; empty symbols, desorption.

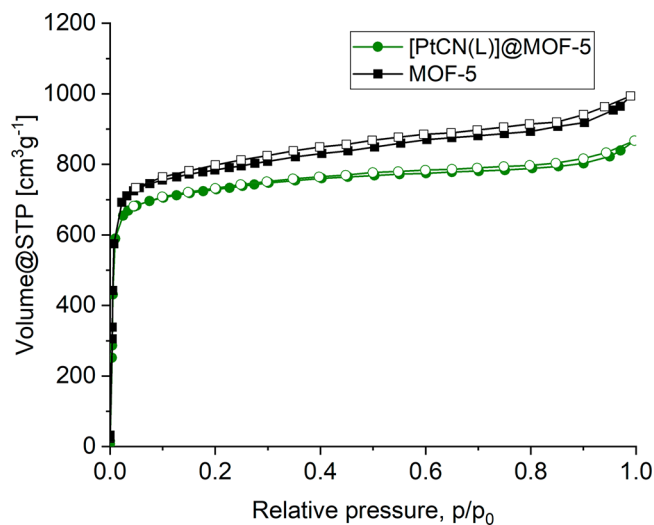


Figure 4. N₂ sorption isotherms of [PtCN(L)]@MOF-5 (green circles; from MOF-5 powders) and neat MOF-5 (black squares). Filled symbols, adsorption; open symbols, desorption.

materials,⁶⁴ since N₂ sorption often overestimates BET areas of micro- to mesoporous MOFs.^{65,66}

Up to $p/p_0 \approx 0.2$, the Ar sorption isotherm of ZIF-8 corresponds to a type I isotherm. The Ar sorption isotherm has a pronounced adsorption step at $p/p_0 \approx 0.55$ with a hysteresis loop in the range of 0.3 to 0.6. Again, this second step is due to the reorganization of the linker, causing additional adsorption.⁶⁷

However, the Ar adsorption isotherms and porosity characteristic for neat ZIF-8 and its composites are nearly the same within experimental uncertainty (Figure 3, Table 2). This seems at first counterintuitive to a successful encapsulation of the complex; however other analytical methods including atomic absorption spectroscopy (Table S7) and photoluminescence spectroscopy (Figure 5) clearly show that the complexes are encapsulated up to ~ 2.3 wt % in all ZIF-8 samples. Neat ZIF-8 porosity data from Ar sorption span a range from $989 \text{ m}^2 \text{ g}^{-1}$ to $1200 \text{ m}^2 \text{ g}^{-1}$ for the specific BET surface area depending *inter alia* on the synthesis conditions. Although the pore size of ZIF-8 may seem to be large enough to accommodate the Pt complexes, it must be clear that in solution the dissolved Pt(II) complex will have a solvent shell, leading to a higher effective radius than its dimensions inferred from the crystal structure. Hence, during the *in situ* formation of ZIF-8, the framework will construct around the solvated Pt complexes. Most likely, perfect ZIF-8 pores or a perfect ZIF-8 framework cannot be generated around the solvated complex, but a ZIF-8 defect structure will be obtained, leading to the formation of “super-pore” defects in which the solvated Pt(II) complex is embedded (Figure S64). When the complex@ZIF-8 product is dried after synthesis, the solvate shell is evaporated, resulting in a super pore “rattle” with the complex inside. It has been shown for ZIF-8 that synthesis procedures which lead to the targeted addition of defects in the ZIF-8 structure increase the surface area by 100 to $250 \text{ m}^2 \text{ g}^{-1}$ (and also the pore volume).^{70,71} Also, additional reactants can change the ZIF-8 surface area.⁷² Here, the *in situ* synthesis of the complex@ZIF-8 composites requires slightly inherent differences in the synthesis conditions from the neat ZIF-8. In light of what has been stated before, it is evident that a direct porosity comparison between neat ZIF-8 and its composite is difficult. The inclusion of small complex molecules into a MOF should only lead to a lower surface area when the molecules fill the pores completely or only block the pore access. In our case, however, we must assume a superpore or defect-structure formation around the complex such that the surface area could even increase. The “unchanged” surface area is interpreted through the opposing effects of such a surface area increase and the incorporation of an additional “dead mass,” which reduces the specific (mass-based) surface area. We note again that our other analyses, that is, atomic absorption spectroscopy

Table 2. Porosity Characteristics of the complex@MOF Composites and Neat MOFs

	sample ^a	BET [$\text{m}^2 \text{ g}^{-1}$]	maximum uptake ^b [$\text{cm}^3 \text{ g}^{-1}$]	micropore volume ^c [$\text{cm}^3 \text{ g}^{-1}$]	total pore volume ^d [$\text{cm}^3 \text{ g}^{-1}$]
Ar sorption	[PtCN(L)]@ZIF-8-5	1387	555	0.4	0.74
	[PtCl(L)]@ZIF-8	1368	538	0.4	0.71
	ZIF-8	1384 (lit.: 989–1200) ^{68,69}	560	0.4	0.75
N ₂ sorption	[PtCN(L)]@MOF-5	2894	788	0.9	1.2
	[PtCl(L)]@MOF-5	2877	773	0.9	1.2
	MOF-5	3060 (lit.: 2900) ⁷³	893	1.0	1.4

^a“5” indicates the amount of Pt(II) complex used in the ZIF-8 composite synthesis; MOF-5 composites from MOF-5 powder sample.

^bDetermined at $p/p_0 = 0.65$ for ZIF-8 and 0.8 for MOF-5. ^cDetermined at a $p/p_0 = 0.1$ –0.2 for pores <12 nm for ZIF-8 and <15 nm for MOF-5.

^dDetermined at a $p/p_0 = 0.8$ for pores <12 nm for ZIF-8 and $p/p_0 = 0.85$ for pores <15 nm for MOF-5.

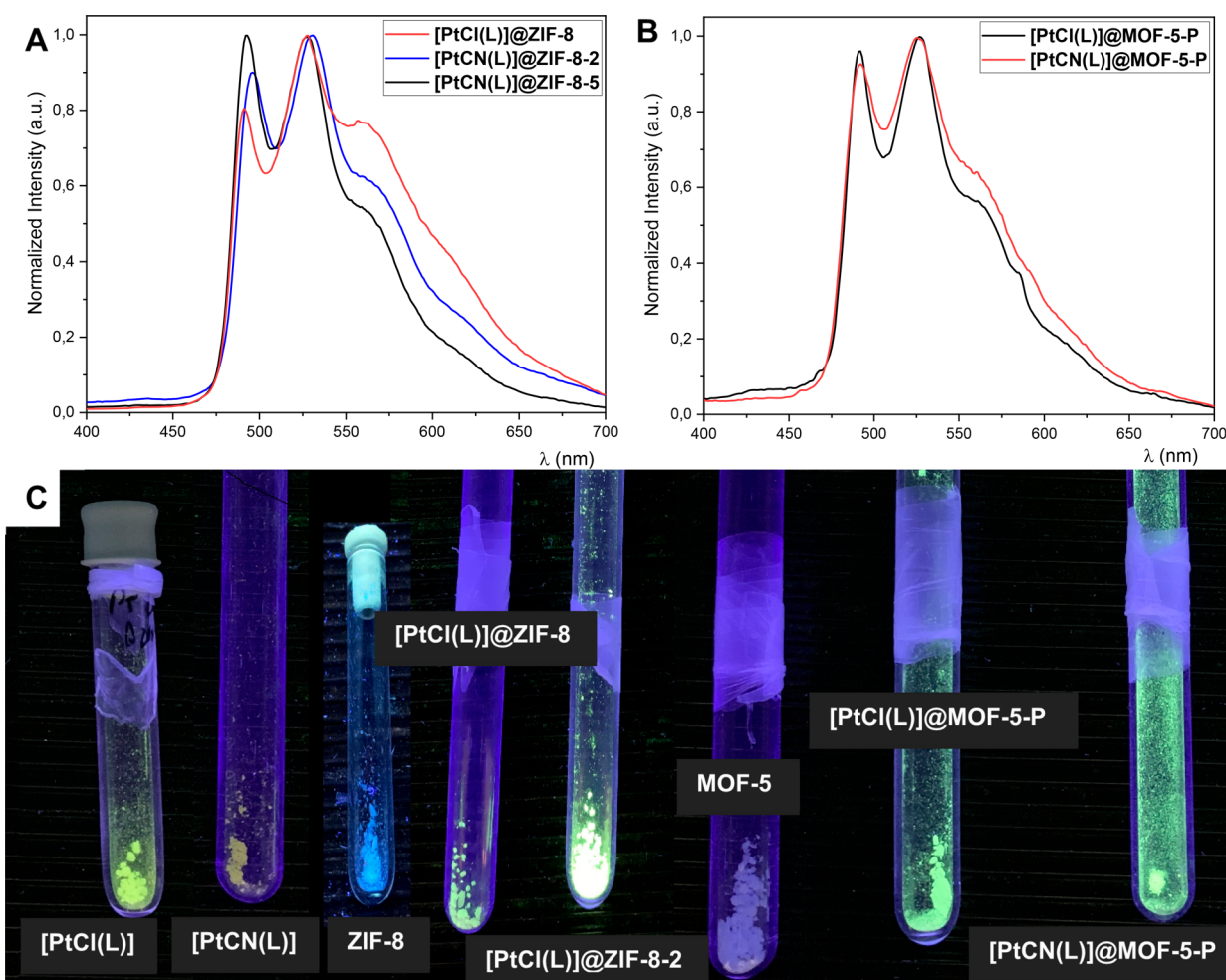


Figure 5. (A) Emission spectra ($\lambda_{\text{exc}} = 350$ nm) of [PtCl(L)]@ZIF-8 (red), [PtCN(L)]@ZIF-8-2 (blue), and [PtCN(L)]@ZIF-8-5 (black) at room temperature (“-2” and “-5” in ZIF-8-2, ZIF-8-5 indicate the amount of Pt complex in mg, which was used in the composite synthesis). (B) Emission spectra ($\lambda_{\text{exc}} = 350$ nm) of [PtCl(L)]@MOF-5-P (Powder, black) and [PtCN(L)]@MOF-5-P (Powder, red; “P” denotes powder sample). (C) Picture ($\lambda_{\text{exc}} = 366$ nm) of the pure solid complexes (left), pure ZIF-8, and its composites with complexes (middle) as well as pure MOF-5 and its composites with both complexes (right; samples under Ar atmosphere).

and the photophysical data, clearly confirm the successful encapsulation of the Pt complexes in ZIF-8.

For MOF-5, a porosity comparison was possible by using a sample from the same batch for the neat MOF and its postsynthetically derived composites. For the MOF-5 samples, all measurements gave a type I isotherm typical for microporous materials. The BET-surface area of neat MOF-5 was determined as $3060 \text{ m}^2 \text{ g}^{-1}$ from N_2 adsorption (Figure 4), which is in good agreement with the literature values ($2200\text{--}2900 \text{ m}^2 \text{ g}^{-1}$).^{73–75} As expected, the BET-surface areas of the composites derived from MOF-5 are slightly lower than the BET-surface area of neat MOF-5 (Table 2). Despite the somewhat larger amount of complex encapsulated postsynthetically for MOF-5 (as compared to the ZIF-8 composites and reaching up to ~ 3.7 wt %, see Table S8), only slightly lower BET surface area and pore volumes are observed for the complex@MOF-5 composites (Table 2).

Scanning Electron Microscopy of complex@MOF Composites. Scanning electron micrographs of [PtCN(L)]@ZIF-8-5 (Figure 6, top) and [PtCl(L)]@ZIF-8 as well as neat ZIF-8 (Figures S65 and S66) show small spherical particles with an approximate diameter of $83 \text{ nm} \pm 14$ and $90 \text{ nm} \pm 14$ nm, respectively (histograms shown in Figures S67

and S68). Within the range of the standard deviation, the particles have the same size as neat ZIF-8 corresponding to $92 \text{ nm} \pm 14$ nm (Figures S66 and S69). Thus, the *in situ* encapsulation has no measurable effect on the crystal growth or size, supporting the results from the PXRD measurement. For MOF-5, the SEM images and the particle size distribution of $2 \mu\text{m} \pm 1 \mu\text{m}$ derived therefrom agree between neat MOF-5 and its composites (Figure 6, bottom, and Figures S70–S74). All SEM images show a small number of particles that are significantly larger than the average.

Quantification of Metals in the complex@MOF Composites. The amount of the encapsulated Pt(II) complexes in ZIF-8 and MOF-5 was determined by Pt and Zn quantification using a graphite furnace and flame atomic absorption spectroscopy (GFAAS and FAAS), respectively (Tables S7 and S8). For small amounts (below 1 wt %), the AAS determination of Pt showed that the loading can vary significantly between batches, indicating a less reproducible incorporation but possibly also sample inhomogeneities or larger uncertainties in the AAS sample preparation.

The Pt quantification becomes reproducible at about 2 and 3 wt % of the [PtCN(L)] complex in ZIF-8 (prepared with 5 mg and 10 mg of complex, respectively, during the *in situ*

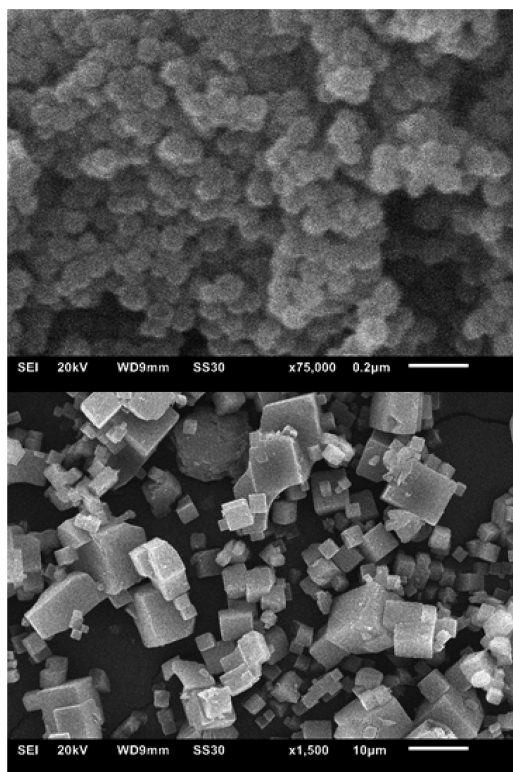


Figure 6. SEM image of [PtCN(L)]@ZIF-8-5 (top; prepared from 5 mg of Pt(II) complex) and [PtCN(L)]@MOF-5 (bottom).

encapsulation). This corresponds to a maximum loading of one Pt atom per 70 Zn atoms for ZIF-8, while starting from a molar Pt to Zn ratio corresponding to 5:70. In comparison, the [PtCl(L)]@ZIF-8 sample contains significantly less complex (<1 wt %) than the [PtCN(L)]@ZIF-8-5 sample (2 wt %) if the same amount of complex (5 mg) is used in the synthesis. Therefore, [PtCN(L)] seems to be more suitable for encapsulation into ZIF-8, possibly due to interactions between the cyanido ligand and methylimidazole, or due to slightly better solubility of [PtCN(L)] in methanol. If the amount of complex used in the synthesis is increased, also the mass fraction of complex in the product increases, albeit not proportionally. With only 1 or 2 mg of [PtCN(L)] during the synthesis, the composite loading was less than 1 wt %. For 5 mg of [PtCN(L)] during the synthesis, a composite loading of ~2 wt % and, for 10 mg, a loading of ~3 wt % was achieved.

In MOF-5, Pt was detected in significant amounts for all composite samples. Again, [PtCN(L)] seems to be more suitable for encapsulation in MOF-5 than [PtCl(L)], possibly due to interactions between the cyanido unit and Zn^{2+} or the structural MOF-ligand, or even due to the slightly better solubility of [PtCN(L)] in methanol. The amount of [PtCN(L)] (roughly 3.7 wt % \pm 0.5 wt %) in the composites obtained from MOF-5 powders is more than 10 times higher than for [PtCl(L)] (approximately 0.30 wt % \pm 0.03 wt %) using the same loading conditions. For the complex@MOF-5 composites derived from single crystals of MOF-5, the amount of encapsulated [PtCN(L)] in the three to four preselected crystals is significantly lower (only 0.37 wt % \pm 0.05 wt %) if compared to about the same mass of powder. This can be traced to the longer diffusion paths of the larger cubic single crystals (edge length 0.5 mm to 1 mm) if compared to the smaller powder particles. For [PtCl(L)], this effect is even

stronger, with only 0.003 wt % \pm 0.001 wt % effectively encapsulated. The longer diffusion path in the single crystals can be blocked by complexes that become immobilized near the pore mouths (*vide infra*).

DFT Calculations on [PtCN(L)]@MOF-5 Composites.

For a visualization of the complex in a MOF matrix, the complex was placed in the middle of the pore and the system was allowed to fully relax, resulting in the structure shown in Figure 7. It is evident upon visual inspection that only a

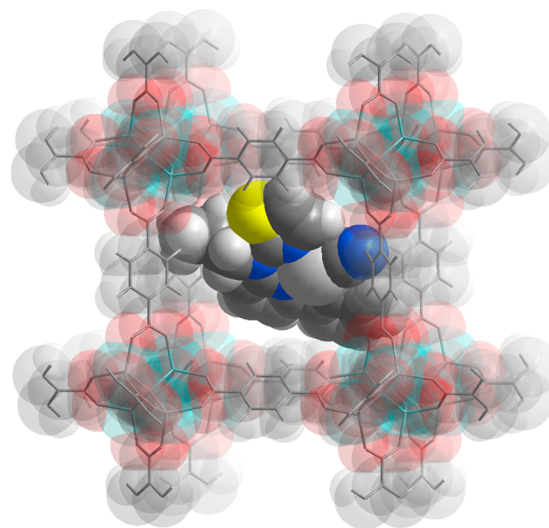


Figure 7. Visualization of one possible structure of [PtCN(L)]@MOF-5. Positioning of the complex was calculated with DFT methods. The binding energy between the complex and MOF-5 is 76.54 kJ mol⁻¹.

monomeric entity of the complex can fit approximately along the room diagonal of the cubic pore in MOF-5. The binding energy of [PtCN(L)] to MOF-5 was obtained as the difference between the sum of energies of MOF-5 and [PtCN(L)] alone and the energy of the composite, where the energy of [PtCN(L)] alone was obtained by placing the complex structure in a cell of the same size as found in MOF-5. The method resulted in a binding energy of 76.54 kJ mol⁻¹. Details on the computational setup can be found in the SI.

Confocal Laser Scanning Microscopy of the complex@MOF-5 Composites. To visualize and thereby prove the encapsulation of the complexes in the MOF-5 single crystals, [PtCN(L)]@MOF-5 and [PtCl(L)]@MOF-5 were imaged with confocal laser scanning microscopy (CLSM). For [PtCN(L)]@MOF-5, the encapsulation of the complex at the outer regions of the crystal can be verified (Figure 8). The inner region of the crystal gives no luminescence, supporting the hypothesis that the complexes become immobilized near the pore mouths. The bright luminescence spots extend up to 200 μ m into the crystal, indicating that the complex has penetrated by diffusion and is encapsulated in the pores. Due to the small amount of [PtCl(L)] complex encapsulated in the single crystals of MOF-5 (see AAS results, Table S8), the CLSM images show only a weak luminescence intensity from the complex, and fluorescence of the MOF itself can be detected in the background as well (Figures S75, left, and S76). Therefore, these images give no information about internal or external immobilization of the complex.

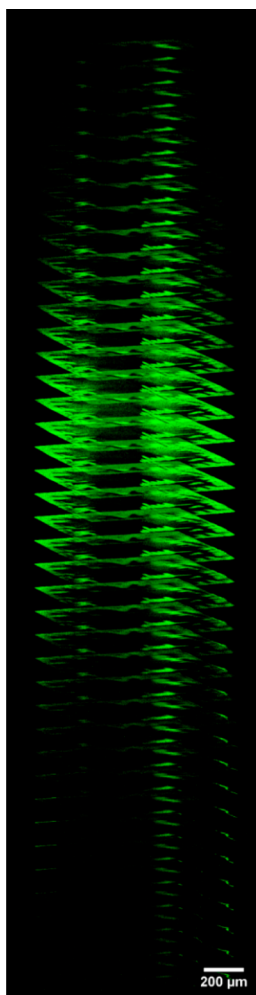


Figure 8. CLSM image of a single crystal of [PtCN(L)]@MOF-5. The crystal was scanned in the top-to-bottom (z) direction in steps of $0.1 \mu\text{m}$. The obtained images were stacked to visualize the 3D scan (see Figure S77, SI for the individual images in an on-top view). $\lambda_{\text{exc}} = 405 \text{ nm}$, $\lambda_{\text{em}} = 550 \text{ nm}$. A laser power of 5% did not cause a significant MOF background photoluminescence.

Photophysical Characterization of the complex@MOF Composites. The photophysical data of the composites are summarized in Table 3 and the corresponding photoluminescence spectra are depicted in Figure 5 and Figures S79–S101. The ZIF-8 composite prepared with 5 mg of [PtCl(L)] has the lowest Pt loading, the resulting emission spectrum is shown in Figure 5A. The emission and excitation spectra resemble those in solution, whereas $\tau = 5.4 \mu\text{s}$ is closer to the neat solid-state form of the complex. In fact, these values correspond neither to the solid state nor to glassy matrices of the complex alone. The low Φ_{L} in air (≤ 0.04) resembles the neat solid complex. In an Ar atmosphere, the Φ_{L} rises to 0.07, proving that, unlike the pure complex, the emission of the composite is significantly quenched by $^3\text{O}_2$.

Even though [PtCN(L)]@ZIF-8 gave the highest loading efficiency when 5 mg of the complex was present during the encapsulation and yielding [PtCN(L)]@ZIF-8-5, the best photophysical performance was observed for the composite resulting from 2 mg of complex ([PtCN(L)]@ZIF-8-2). This is most likely related to intermolecular quenching at higher concentrations, whereas at the lowest loadings the uncertainty is higher when the Φ_{L} is determined, mostly due to a poorer

signal-to-noise-ratio associated with weaker photoluminescence intensities. For the lower loadings, the emission clearly originates from purely monomeric species (Figure 5B). In fact, the *in situ* synthesis toward complex@ZIF-8 can potentially lead to the encapsulation of aggregates into defect regions with enlarged pores. Nonetheless, MOFs and related structures are known for the prevention of the aggregation of fluorescent organic dyes.^{26,76,77} Due to the consistent shape of the emission spectra, we conclude that there is no significant interaction of the complexes with the MOF components. For [PtCN(L)]@ZIF-8-2, the lower loading leads to an enhanced lifetime ($\tau = 18.3 \mu\text{s}$) and to a boost of Φ_{L} reaching 0.29 in an Ar atmosphere, if compared with the solid state of the pure complex. It is worth it to mention that both the Φ_{L} and the τ are strongly dependent on the presence of $^3\text{O}_2$. In fact, the air-equilibrated sample of the composite shows significantly shortened τ and lowered Φ_{L} ($\tau = 3.4 \mu\text{s}$ and $\Phi_{\text{L}} < 0.02$, respectively). These values are comparable to those of the neat complex in the solid state at room temperature. Higher loadings in the ZIF-8 composites (prepared by using 5–10 mg of complex) lead to drops in Φ_{L} and shortened τ , with a shift in the vibrational progression and an enhancement in the intensity of the emission band at $\lambda = 560 \text{ nm}$ (Figure 5 A), which was previously assigned to the excimeric luminescence from dimeric species.

Due to the sensitivity of MOF-5 to humidity, the photophysical measurements were carried out in a dry Ar atmosphere (for the powders in the spectrometer) or in *n*-hexane and emulsion oil (for the single crystals on the confocal time-resolved microscope with spectral resolution). The vibrational progression observed in the emission spectra suggests a monomer-based photoluminescence (Figure 5B). This observation is in good agreement with the results from DFT calculations showing that only monomeric species can fit into MOF-5 cavities approximately along the pore diagonal (Figure 7). Compared to the complexes as pure solids, the composites show similarly long τ values. For the [PtCl(L)]@MOF-5 composite as a powder, the Φ_{L} is actually lower (≤ 0.04) than in the solid state ($\Phi_{\text{L}} = 0.04$) but still higher than in fluid DCM solution at room temperature ($\Phi_{\text{L}} < 0.02$). The composite [PtCN(L)]@MOF-5 shows a better Φ_{L} (0.08) than the pure solid complex ($\Phi_{\text{L}} \leq 0.04$), which is most likely due to the monomeric nature and the lack of intermolecular quenching in MOF-5, but still inferior to the complex in fluid deaerated DCM solution at room temperature ($\Phi_{\text{L}} = 0.46$). For both complexes, the single crystals of MOF-5 show very low loadings (see Table S8), and also the τ values (4.7 and $4.04 \mu\text{s}$) are shorter than for MOF-5 composites obtained from powders (11.1 and $10.5 \mu\text{s}$).

In general, the photoluminescence decays of the composites are triexponential. The two longer components resemble the τ of the pure complexes in frozen glassy matrices at 77 K, where vibrational relaxation is restricted leading to longer decays and enhanced Φ_{L} . In contrast, the shorter components are closer to the τ in pure solids. The [PtCN(L)]-based composites show that higher loadings favor shorter decays, thus suggesting intermolecular quenching.

EXPERIMENTAL SECTION

General information about experimental procedures including instrumental and synthetic methods, structural characterization of the ligand precursors, and the complexes as well as preparation of the composites are provided in the Supporting Information.

Table 3. Photophysical Data for the Complexes [PtCl(L)] and [PtCN(L)] in the Composites

composite ^a	$\tau/\mu\text{s}^b$		$\Phi \pm 0.02^b$	
	air	Ar	air	Ar
[PtCl(L)]@ZIF-8	5.2 ± 0.8 [22.7 ± 1.1 (9); 6.2 ± 0.3 (40); 1.6 ± 0.3 (52)]	5.4 ± 0.5 [17.3 ± 0.5 (12); 6.3 ± 0.2 (40); 1.52 ± 0.17 (48)]	<0.02	0.07
[PtCN(L)]@ZIF-8-1	4.9 ± 0.8 [18.7 ± 0.5 (10); 5.78 ± 0.18 (38); 1.62 ± 0.13 (52)]	17.7 ± 1.4 [40.7 ± 0.9 (17); 17.1 ± 0.5 (54); 4.6 ± 0.8 (29)]	<0.02	0.08
[PtCN(L)]@ZIF-8-2	3.4 ± 0.5 [21.6 ± 1.0 (6); 5.0 ± 0.3 (31); 1.01 ± 0.12 (64)]	18.3 ± 1.3 [51.2 ± 1.0 (15); 18.9 ± 0.5 (45); 5.3 ± 0.6 (40)]	<0.02	0.29
[PtCN(L)]@ZIF-8-5	3.8 ± 0.6 [17.5 ± 0.4 (8); 4.63 ± 0.13 (38); 1.08 ± 0.09 (54)]	8.5 ± 1.1 [32.7 ± 1.2 (11); 9.6 ± 0.5 (39); 2.5 ± 0.4 (50)]	<0.02	0.16
[PtCN(L)]@ZIF-8-10	2.8 ± 0.5 [17.0 ± 1.2 (5); 4.11 ± 0.14 (31); 1.0 ± 0.3 (63)]	7.9 ± 0.8 [28.8 ± 0.9 (10); 9.3 ± 0.4 (41); 2.5 ± 0.3 (49)]	<0.02	0.06
[PtCl(L)]@MOF-5 (as powder)	n.d.	11.1 ± 1.3 [58 ± 2 (6); 17.4 ± 0.8 (30); 3.9 ± 0.4 (64)]	n.d.	0.02
[PtCN(L)]@MOF-5 (as powder)	n.d.	10.5 ± 1.0 [30.4 ± 0.8 (14); 10.4 ± 0.4 (49); 3.2 ± 0.5 (37)]	n.d.	0.08
[PtCl(L)]@MOF-5 (as single crystals)	n.d.	4.7 ± 0.4 [8.6 ± 0.7 (50); 1.33 ± 0.16 (31); 0.10 ± 0.02 (19)]	n.d.	n.d.
[PtCN(L)]@MOF-5 (as single crystals)	n.d.	4.04 ± 0.16 [11.7 ± 0.4 (19); 3.29 ± 0.16 (45); 0.83 ± 0.04 (36)]	n.d.	n.d.

^a“-1” to “-10” in ZIF-8 composites denote the amount of complex in mg (i.e., 1 mg -10 mg) used in the encapsulation process. ^bFor multiexponential decays, the amplitude-weighted average lifetime is given as well as the different components in square brackets with their relative amplitudes in parentheses. Humidity-sensitive samples were not measured in air-equilibrated environments (n.d.); single crystal samples of MOF-5 composites were not measurable with our equipment (n.d.). $\lambda_{\text{exc}} = 350$ nm was used for the Φ_L measurement, and $\lambda_{\text{exc}} = 376.7$ nm and $\lambda_{\text{em}} = 530$ nm were used for the time-resolved photoluminescence decay measurements.

CONCLUSION

The synthesis of two tailored cyclometalated Pt(II) complexes bearing a new monoanionic C^NN^N pincer luminophore was achieved, showing that exchange of the monodentate anionic coligand can prolong the τ while boosting the Φ_L . Furthermore, these complexes were encapsulated in two different MOF scaffolds providing a rigid “solid-solution” environment that enhances their phosphorescence and suppresses intermolecular quenching. Due to the porous structure and the long-lived phosphorescence from the excited triplet states, the emission of these composites shows sensitivity to ³O₂. The best results were obtained by *in situ* encapsulation of the cyanido complex into the highly stable ZIF-8 at lower loadings, thus precluding intermolecular quenching. On the other hand, MOF-5 is sensitive to humidity, and the postsynthetic encapsulation of the complexes led to worse photoluminescence efficiencies. These results provide an elegant approach to increase the efficiency of weakly emissive coordination compounds able to perform as triplet emitters at room temperature thanks to a rigid confined environment resembling frozen glassy matrices. The sensitivity to ³O₂ and the fact that the ZIF-8 composites are stable and easier to handle than solutions or frozen matrices could lead to potential applications as robust ³O₂ sensors or as catalysts for ¹O₂-mediated photooxidations.

ASSOCIATED CONTENT

Supporting Information

The Supporting Information is available free of charge at <https://pubs.acs.org/doi/10.1021/acs.inorgchem.0c00678>.

Synthetic and computational procedures, the structural characterization as well as the photophysical data of every compound and composite; for the composites, BET and PXRD graphs, SEM and CLSM pictures, and the AAS measurements (PDF)

Accession Codes

CCDC 1978467–1978470 contain the supplementary crystallographic data for this paper. These data can be obtained free of charge via www.ccdc.cam.ac.uk/data_request/cif, or by emailing data_request@ccdc.cam.ac.uk, or by contacting The Cambridge Crystallographic Data Centre, 12 Union Road, Cambridge CB2 1EZ, UK; fax: +44 1223 336033.

AUTHOR INFORMATION

Corresponding Authors

Christoph Janiak – Institut für Anorganische Chemie und Strukturchemie, Heinrich-Heine-Universität Düsseldorf, 40225 Düsseldorf, Germany; orcid.org/0000-0002-1964-0169; Email: janiak@uni-duesseldorf.de

Cristian A. Strassert – CiMIC, SoN, Institut für Anorganische und Analytische Chemie and CeNTech, Westfälische Wilhelms-Universität Münster, 48149 Münster, Germany; orcid.org/0000-0002-6288-9605; Email: ca.s@wwu.de

Authors

Tim-Oliver Knedel – Institut für Anorganische Chemie und Strukturchemie, Heinrich-Heine-Universität Düsseldorf, 40225 Düsseldorf, Germany

Stefan Buss – CiMIC, SoN, Institut für Anorganische und Analytische Chemie and CeNTech, Westfälische Wilhelms-Universität Münster, 48149 Münster, Germany

Iván Maisuls – CiMIC, SoN, Institut für Anorganische und Analytische Chemie and CeNTech, Westfälische Wilhelms-Universität Münster, 48149 Münster, Germany

Constantin G. Daniliuc – Organisch-Chemisches Institut, Westfälische Wilhelms-Universität Münster, 48149 Münster, Germany

Carsten Schlüsener – Institut für Anorganische Chemie und Strukturchemie, Heinrich-Heine-Universität Düsseldorf, 40225 Düsseldorf, Germany

Philipp Brandt – Institut für Anorganische Chemie und Strukturchemie, Heinrich-Heine-Universität Düsseldorf, 40225 Düsseldorf, Germany

Oliver Weingart – Institut für Theoretische Chemie und Computerchemie, Heinrich-Heine-Universität Düsseldorf, 40225 Düsseldorf, Germany

Annette Vollrath – Institut für Anorganische Chemie und Strukturchemie, Heinrich-Heine-Universität Düsseldorf, 40225 Düsseldorf, Germany

Complete contact information is available at:

<https://pubs.acs.org/10.1021/acs.inorgchem.0c00678>

Author Contributions

*T.-O.K. and S.B. contributed equally to this work

Notes

The authors declare no competing financial interest.

ACKNOWLEDGMENTS

The work of O.W. and C.J. was supported by the Deutsche Forschungsgemeinschaft (DFG) - 396890929 / GRK 2482. C.A.S. would like to gratefully acknowledge the Deutsche Forschungsgemeinschaft for generous financial support (DFG: EXC1003 "Cells in Motion"; TRR61 - project STR 1186/7-1; Priority Program LCRMC - project STR 1186/6-1). I.M. acknowledges the WWU and the Alexander von Humboldt Foundation for the postdoctoral fellowships.

REFERENCES

- (1) Zhong, J.-J.; Meng, Q.-Y.; Wang, G.-X.; Liu, Q.; Chen, B.; Feng, K.; Tung, C.-H.; Wu, L.-Z. A Highly Efficient and Selective Aerobic Cross-Dehydrogenative-Coupling Reaction Photocatalyzed by a Platinum(II) Terpyridyl Complex. *Chem. - Eur. J.* **2013**, *19*, 6443–6450.
- (2) Chow, P.-K.; Cheng, G.; Tong, G. S. M.; To, W.-P.; Kwong, W.-L.; Low, K.-H.; Kwok, C.-C.; Ma, C.; Che, C.-M. Luminescent Pincer Platinum(II) Complexes with Emission Quantum Yields up to Almost Unity: Photophysics, Photoreductive C-C Bond Formation, and Materials Applications. *Angew. Chem., Int. Ed.* **2015**, *54*, 2084–2089.
- (3) Wu, P.; Wong, E. L.-M.; Ma, D.-L.; Tong, G. S.-M.; Ng, K.-M.; Che, C.-M. Cyclometalated Platinum(II) Complexes as Highly Sensitive Luminescent Switch-On Probes for Practical Application in Protein Staining and Cell Imaging. *Chem. - Eur. J.* **2009**, *15*, 3652–3656.
- (4) Chung, C. Y.-S.; Li, S. P.-Y.; Louie, M.-W.; Lo, K. K.-W.; Yam, V. W.-W. Induced Self-Assembly and Disassembly of Water-Soluble Alkynylplatinum(II) Terpyridyl Complexes with "Switchable" Near-Infrared (NIR) Emission Modulated by Metal-Metal Interaction over Physiological pH: Demonstration of pH-Responsive NIR Luminescent Probes in Cell-Imaging Studies. *Chem. Sci.* **2013**, *4*, 2453–2462.
- (5) Baggaley, E.; Botchway, S. W.; Haycock, J. W.; Morris, H.; Sazanovich, I. V.; Williams, J. A. G.; Weinstein, J. A. Long-Lived Metal Complexes open up Microsecond Lifetime Imaging Microscopy under Multiphoton Excitation: from FLIM to PLIM and beyond. *Chem. Sci.* **2014**, *5*, 879–886.
- (6) Zou, T.; Liu, J.; Lum, C. T.; Ma, C.; Chan, R. C.-T.; Lok, C.-N.; Kwok, W.-M.; Che, C.-M. Luminescent Cyclometalated Platinum(II) Complex Forms Emissive Intercalating Adducts with Double-Stranded DNA and RNA: Differential Emissions and Anticancer Activities. *Angew. Chem., Int. Ed.* **2014**, *53*, 10119–10123.
- (7) Ma, D.-L.; Shum, T. Y.-T.; Zhang, F.; Che, C.-M.; Yang, M. Water Soluble Luminescent Platinum Terpyridine Complexes with Glycosylated Acetylaldehyde and Arylacetylaldehyde Ligands: Photoluminescent Properties and Cytotoxicities. *Chem. Commun.* **2005**, 4675–4677.
- (8) Nisic, F.; Colombo, A.; Dragonetti, C.; Roberto, D.; Valore, A.; Malicka, J. M.; Cocchi, M.; Freeman, G. R.; Williams, J. A. G. Platinum(II) Complexes with Cyclometalated 5- π -delocalized-donor-1,3-di(2-pyridyl)benzene Ligands as Efficient Phosphors for NIR-OLEDs. *J. Mater. Chem. C* **2014**, *2*, 1791–1800.
- (9) Tam, A. Y.-Y.; Tsang, D. P.-K.; Chan, M.-Y.; Zhu, N.; Yam, V. W.-W. A Luminescent Cyclometalated Platinum(II) Complex and its Green Organic Light Emitting Device with High Device Performance. *Chem. Commun.* **2011**, *47*, 3383–3385.
- (10) Sanning, J.; Stegemann, L.; Ewen, P. R.; Schwermann, C.; Daniliuc, C. G.; Zhang, D.; Lin, N.; Duan, L.; Wegner, D.; Doltsinis, N. L.; Strassert, C. A. Colour-Tunable Asymmetric Cyclometalated Pt(II) Complexes and STM-Assisted Stability Assessment of Ancillary Ligands for OLEDs. *J. Mater. Chem. C* **2016**, *4*, 2560–2565.
- (11) Lu, W.; Mi, B.-X.; Chan, M. C. W.; Hui, Z.; Zhu, N.; Lee, S.-T.; Che, C.-M. [(C^NN)Pt(C \equiv C)_nR] (HC^NN = 6-aryl-2,2'-bipyridine, n = 1–4, R = aryl, SiMe₃) as a New Class of Light-Emitting Materials and their Applications in Electrophosphorescent Devices. *Chem. Commun.* **2002**, 206–207.
- (12) Haque, A.; Xu, L.; Al-Balushi, R. A.; Al-Suti, M. K.; Ilmi, R.; Guo, Z.; Khan, M. S.; Wong, W.-Y.; Raithby, P. R. Cyclometalated Tridentate Platinum(II) Arylacetylaldehyde Complexes: Old Wine in New Bottles. *Chem. Soc. Rev.* **2019**, *48*, 5547–5563.
- (13) Krause, M.; Kourkoulos, D.; González-Abradelo, D.; Meerholz, K.; Strassert, C. A.; Klein, A. Luminescent Pt(II) Complexes of Tridentate Cyclometalating 2,5-Bis(aryl)pyridine Ligands. *Eur. J. Inorg. Chem.* **2017**, *2017*, 5215–5223.
- (14) Ravindranathan, D.; Vezzu, D. A. K.; Bartolotti, L.; Boyle, P. D.; Huo, S. Improvement in Phosphorescence Efficiency through Tuning of Coordination Geometry of Tridentate Cyclometalated Platinum(II) Complexes. *Inorg. Chem.* **2010**, *49*, 8922–8928.
- (15) Sinn, S.; Biedermann, F.; De Cola, L. Platinum Complex Assemblies as Luminescent Probes and Tags for Drugs and Toxins in Water. *Chem. - Eur. J.* **2017**, *23*, 1965–1971.
- (16) Proetto, M. T.; Sanning, J.; Peterlechner, M.; Thunemann, M.; Stegemann, L.; Sadegh, S.; Devor, A.; Gianneschi, N. C.; Strassert, C. A. Phosphorescent Pt(II) Complexes Spatially Arrayed in Micellar Polymeric Nanoparticles Providing Dual Readout for Multimodal Imaging. *Chem. Commun.* **2019**, *55*, 501–504.
- (17) Aliprandi, A.; Mauro, M.; De Cola, L. Controlling and Imaging Biomimetic Self-Assembly. *Nat. Chem.* **2016**, *8*, 10–15.
- (18) Wilde, S.; Ma, D.; Koch, T.; Bakker, A.; Gonzalez-Abradelo, D.; Stegemann, L.; Daniliuc, C. G.; Fuchs, H.; Gao, H.; Doltsinis, N. L.; Duan, L.; Strassert, C. A. Toward Tunable Electroluminescent Devices by Correlating Function and Submolecular Structure in 3D Crystal, 2D-Confined Monolayers, and Dimers. *ACS Appl. Mater. Interfaces* **2018**, *10*, 22460–22473.
- (19) Demas, J. N.; Harris, E. W.; McBride, R. P. Energy Transfer from Luminescent Transition Metal Complexes to Oxygen. *J. Am. Chem. Soc.* **1977**, *99*, 3547–3551.
- (20) Wang, X.-D.; Wolfbeis, O. S. Optical Methods for Sensing and Imaging Oxygen: Materials, Spectroscopies and Applications. *Chem. Soc. Rev.* **2014**, *43*, 3666–3761.
- (21) Baldo, M. A.; Forrest, S. R. Transient Analysis of Organic Electrophosphorescence: I. Transient Analysis of Triplet Energy Transfer. *Phys. Rev. B: Condens. Matter Mater. Phys.* **2000**, *62*, 10958–10966.
- (22) Kalinowski, J.; Stampor, W.; Mężyk, J.; Cocchi, M.; Virgili, D.; Fattori, V.; Di Marco, P. Quenching Effects in Organic Electrophosphorescence. *Phys. Rev. B: Condens. Matter Mater. Phys.* **2002**, *66*, 235321–1–235321–15.
- (23) Matthes, P. R.; Höller, C. J.; Mai, M.; Heck, J.; Sedlmaier, S. J.; Schmiechen, S.; Feldmann, C.; Schnick, W.; Müller-Buschbaum, K. Luminescence Tuning of MOFs via Ligand to Metal and Metal to Metal Energy Transfer by Co-Doping of ² ∞ [Gd₂Cl₆(bipy)₃]-2bipy with Europium and Terbium. *J. Mater. Chem.* **2012**, *22*, 10179–10187.
- (24) (4) Sun, C.-Y.; To, W.-P.; Hung, F.-F.; Wang, X.-L.; Su, Z.-M.; Che, C.-M. Metal-Organic Framework Composites with Luminescent Pincer Platinum(II) Complexes: ³MMLCT Emission and Photo-induced Dehydrogenation Catalysis. *Chem. Sci.* **2018**, *9*, 2357–2364.
- (25) Müller, M.; Devaux, A.; Yang, C.-H.; De Cola, L.; Fischer, R. A. Highly Emissive Metal-Organic Framework Composites by Host-Guest Chemistry. *Photochem. Photobiol. Sci.* **2010**, *9*, 846–853.

- (26) Sun, C.-Y.; Wang, X.-L.; Zhang, X.; Qin, C.; Li, P.; Su, Z.-M.; Zhu, D.-X.; Shan, G.-G.; Shao, K.-Z.; Wu, H.; Li, J. Efficient and Tunable White-Light Emission of Metal-Organic Frameworks by Iridium-Complex Encapsulation. *Nat. Commun.* **2013**, *4*, 2717–2724.
- (27) Wang, Q.; Astruc, D. State of the Art and Prospects in Metal-Organic Framework (MOF)-Based and MOF-Derived Nanocatalysis. *Chem. Rev.* **2020**, *120* (2), 1438–1511.
- (28) Cui, Y.; Song, T.; Yu, J.; Yang, Y.; Wang, Z.; Qian, G. Dye Encapsulated Metal-Organic Framework for Warm-White LED with High Color-Rendering Index. *Adv. Funct. Mater.* **2015**, *25*, 4796–4802.
- (29) Liang, K.; Coghlan, C. J.; Bell, S. G.; Doonan, C.; Falcaro, P. Enzyme Encapsulation in Zeolitic Imidazolate Frameworks: a Comparison between Controlled Co-Precipitation and Biomimetic Mineralisation. *Chem. Commun.* **2016**, *52*, 473–476.
- (30) Cui, Y.; Li, B.; He, H.; Zhou, W.; Chen, B.; Qian, G. Metal-Organic Frameworks as Platforms for Functional Materials. *Acc. Chem. Res.* **2016**, *49*, 483–493.
- (31) Luz, I.; Rösler, C.; Epp, K.; Llabrés i Xamena, F. X.; Fischer, R. A. Pd@UiO-66-Type MOFs Prepared by Chemical Vapor Infiltration as Shape-Selective Hydrogenation Catalysts. *Eur. J. Inorg. Chem.* **2015**, *2015*, 3904–3912.
- (32) Dalapati, R.; Sakthivel, B.; Dhakshinamoorthy, A.; Buragohain, A.; Bhunia, A.; Janiak, C.; Biswas, S. A Highly Stable Dimethyl-Functionalized Ce(IV)-Based UiO-66 Metal-Organic Framework Material for Gas Sorption and Redox Catalysis. *CrystEngComm* **2016**, *18*, 7855–7864.
- (33) Ding, L.-G.; Yao, B.-J.; Jiang, W.-L.; Li, J.-T.; Fu, Q.-J.; Li, Y.-A.; Liu, Z.-H.; Ma, J.-P.; Dong, Y.-B. Bifunctional Imidazolium-Based Ionic Liquid Decorated UiO-67 Type MOF for Selective CO₂ Adsorption and Catalytic Property for CO₂ Cycloaddition with Epoxides. *Inorg. Chem.* **2017**, *56*, 2337–2344.
- (34) Dong, Z.; Sun, Y.; Chu, J.; Zhang, X.; Deng, H. Multivariate Metal-Organic Frameworks for Dialing-in the Binding and Programming the Release of Drug Molecules. *J. Am. Chem. Soc.* **2017**, *139*, 14209–14216.
- (35) Achmann, S.; Hagen, G.; Kita, J.; Malkowsky, I. M.; Kiener, C.; Moos, R. Metal-Organic Frameworks for Sensing Applications in the Gas Phase. *Sensors* **2009**, *9*, 1574–1589.
- (36) Lu, G.; Hupp, J. T. Metal-organic frameworks as sensors: A ZIF-8 Based Fabry-Pérot Device as a Selective Sensor for Chemical Vapors and Gases. *J. Am. Chem. Soc.* **2010**, *132*, 7832–7833.
- (37) Dou, Z.; Yu, J.; Cui, Y.; Yang, Y.; Wang, Z.; Yang, D.; Qian, G. Luminescent Metal-Organic Framework Films as Highly Sensitive and Fast-Response Oxygen Sensors. *J. Am. Chem. Soc.* **2014**, *136*, 5527–5530.
- (38) Ye, J.-W.; Zhou, H.-L.; Liu, S.-Y.; Cheng, X.-N.; Lin, R.-B.; Qi, X.-L.; Zhang, J.-P.; Chen, X.-M. Encapsulating Pyrene in a Metal-Organic Zeolite for Optical Sensing of Molecular Oxygen. *Chem. Mater.* **2015**, *27*, 8255–8260.
- (39) Zhou, T.; Du, Y.; Borgna, A.; Hong, J.; Wang, Y.; Han, J.; Zhang, W.; Xu, R. Post-Synthesis Modification of a Metal-Organic Framework to Construct a Bifunctional Photocatalyst for Hydrogen Production. *Energy Environ. Sci.* **2013**, *6*, 3229.
- (40) Toyao, T.; Saito, M.; Dohshi, S.; Mochizuki, K.; Iwata, M.; Higashimura, H.; Horiuchi, Y.; Matsuoka, M. Construction of Pt Complex within Zr-based MOF and its Application for Hydrogen Production under Visible-Light Irradiation. *Res. Chem. Intermed.* **2016**, *42*, 7679–7688.
- (41) Hu, X.; Lu, Y.; Dong, C.; Zhao, W.; Wu, X.; Zhou, L.; Chen, L.; Yao, T.; Shi, S. A Ru(II) Polypyridyl Alkyne Complex Based Metal-Organic Frameworks for Combined Photodynamic/Photothermal/Chemo-Therapy. *Chem. - Eur. J.* **2020**, *26*, 1668.
- (42) Zhang, Y.; Fu, H.; Chen, S.; Liu, B.; Sun, W.; Gao, H. Construction of Iridium(III)-Complex-Loaded MOF Nanoplatform Mediated with a Dual-Responsive Polycationic Polymer for Photodynamic Therapy and Cell Imaging. *Chem. Commun.* **2020**, *56*, 762–765.
- (43) Liao, Y.-T.; Nguyen, V. C.; Ishiguro, N.; Young, A. P.; Tsung, C.-K.; Wu, K. C.-W. Engineering a Homogeneous Alloy-Oxide Interface derived from Metal-Organic Frameworks for Selective Oxidation of 5-Hydroxymethylfurfural to 2,5-Furandicarboxylic Acid. *Appl. Catal., B* **2020**, *270*, 118805.
- (44) Liu, X.-Y.; Xing, K.; Li, Y.; Tsung, C.-K.; Li, J. Three Models to Encapsulate Multicomponent Dyes into Nanocrystal Pores: A New Strategy for Generating High-Quality White Light. *J. Am. Chem. Soc.* **2019**, *141*, 14807–14813.
- (45) Lu, G.; Li, S.; Guo, Z.; Farha, O. K.; Hauser, B. G.; Qi, X.; Wang, Y.; Wang, X.; Han, S.; Liu, X.; DuChene, J. S.; Zhang, H.; Zhang, Q.; Chen, X.; Ma, J.; Loo, S. C. J.; Wei, W. D.; Yang, Y.; Hupp, J. T.; Huo, F. Imparting Functionality to a Metal-Organic Framework Material by Controlled Nanoparticle Encapsulation. *Nat. Chem.* **2012**, *4*, 310–316.
- (46) Knedel, T.-O.; Ricklefs, E.; Schlüsener, C.; Urlacher, V. B.; Janiak, C. Laccase Encapsulation in ZIF-8 Metal-Organic Framework Shows Stability Enhancement and Substrate Selectivity. *ChemistryOpen* **2019**, *8*, 1337–1344.
- (47) Liao, F.-S.; Lo, W.-S.; Hsu, Y.-S.; Wu, C.-C.; Wang, S.-C.; Shieh, F.-K.; Morabito, J. V.; Chou, L.-Y.; Wu, K. C.-W.; Tsung, C.-K. Shielding against Unfolding by Embedding Enzymes in Metal-Organic Frameworks via a *de Novo* Approach. *J. Am. Chem. Soc.* **2017**, *139*, 6530–6533.
- (48) Gascón, V.; Castro-Miguel, E.; Díaz-García, M.; Blanco, R. M.; Sanchez-Sanchez, M. In Situ and Post-Synthesis Immobilization of Enzymes on Nanocrystalline MOF Platforms to Yield Active Biocatalysts. *J. Chem. Technol. Biotechnol.* **2017**, *92*, 2583–2593.
- (49) Gascón, V.; Jiménez, M. B.; Blanco, R. M.; Sanchez-Sanchez, M. Semi-Crystalline Fe-BTC MOF Material as an Efficient Support for Enzyme Immobilization. *Catal. Today* **2018**, *304*, 119–126.
- (50) Patil, P. D.; Yadav, G. D. Rapid In Situ Encapsulation of Laccase into Metal-Organic Framework Support (ZIF-8) under Biocompatible Conditions. *ChemistrySelect* **2018**, *3*, 4669–4675.
- (51) Naseri, M.; Pitzalis, F.; Carucci, C.; Medda, L.; Fotouhi, L.; Magner, E.; Salis, A. Lipase and Laccase Encapsulated on Zeolite Imidazolate Framework: Enzyme Activity and Stability from Voltammetric Measurements. *ChemCatChem* **2018**, *10*, 5425–5433.
- (52) Yam, V. W.-W.; Tang, R. P.-L.; Wong, K. M.-C.; Cheung, K.-K. Synthesis, Luminescence, Electrochemistry, and Ion-Binding Studies of Platinum(II) Terpyridyl Acetylide Complexes. *Organometallics* **2001**, *20*, 4476–4482.
- (53) Wilson, M. H.; Ledwaba, L. P.; Field, J. S.; McMillin, D. R. Push-Pull Effects and Emission from Ternary Complexes of Platinum(II), Substituted Terpyridines, and the Strong-Field Cyanide Ion. *Dalton Trans.* **2005**, 2754–2759.
- (54) Li, H.; Eddaoudi, M.; O’Keeffe, M.; Yaghi, O. M. Design and Synthesis of an Exceptionally Stable and Highly Porous Metal-Organic Framework. *Nature* **1999**, *402*, 276–279.
- (55) Huang, X.-C.; Lin, Y.-Y.; Zhang, J.-P.; Chen, X.-M. Ligand-Directed Strategy for Zeolite-Type Metal-Organic Frameworks: Zinc(II) Imidazolates with Unusual Zeolitic Topologies. *Angew. Chem., Int. Ed.* **2006**, *45*, 1557–1559.
- (56) Schnürch, M.; Waldner, B.; Hilber, K.; Mihovilovic, M. D. Synthesis of 5-arylated *N*-arylthiazole-2-amines as Potential Skeletal Muscle Cell Differentiation Promoters. *Bioorg. Med. Chem. Lett.* **2011**, *21*, 2149–2154.
- (57) Dao-Huy, T.; Waldner, B.; Wimmer, L.; Schnürch, M.; Mihovilovic, M. D. Synthesis of *endo*- and *exo*-*N*-Protected 5-Arylated 2-Aminothiazols through Direct Arylation: An Efficient Route to Cell Differentiation Accelerators. *Eur. J. Org. Chem.* **2015**, *2015*, 4765–4771.
- (58) Janiak, C. A critical Account on pi-pi Stacking in Metal Complexes with Aromatic Nitrogen-containing Ligands. *J. Chem. Soc., Dalton Trans.* **2000**, 3885–3896.
- (59) (a) Nishio, M. The CH/π Hydrogen Bond in Chemistry. Conformation, Supramolecules, Optical Resolution and Interactions Involving Carbohydrates. *Phys. Chem. Chem. Phys.* **2011**, *13*, 13873–13900. (b) Nishio, M.; Umezawa, Y.; Honda, K.; Tsuboyama, S.;

- Suezawa, H. CH/ π Hydrogen Bonds in Organic and Organometallic Chemistry. *CrystEngComm* **2009**, *11*, 1757–1788. (c) Nishio, M. CH/ π Hydrogen Bonds in Crystals. *CrystEngComm* **2004**, *6*, 130–158. (d) Janiak, C.; Temizdemir, S.; Dechert, S.; Deck, W.; Girgsdies, F.; Heinze, J.; Kolm, M.J.; Scharmann, T.G.; Zipfel, O.M. Binary [Hydrotris(indazol-1-yl)borato]metal Complexes, M(Tp^B)₂^[1] with M = Fe, Co, Ni, Cu, and Zn: Electronic Properties and Solvent-Dependent Framework Structures through C–H \cdots π Interactions. *Eur. J. Inorg. Chem.* **2000**, *2000*, 1229–1241. (e) Umezawa, Y.; Tsuboyama, S.; Honda, K.; Uzawa, J.; Nishio, M. CH/ π Interaction in the Crystal Structure of Organic Compounds. A Database Study. *Bull. Chem. Soc. Jpn.* **1998**, *71*, 1207–1213. (f) Nishio, M. H.; Hirota, M.; Umezawa, Y. *The CH/ π Interaction (Evidence, Nature and Consequences)*; Wiley-VCH, New York, 1998.
- (60) Park, K. S.; Ni, Z.; Cote, A. P.; Choi, J. Y.; Huang, R.; Uribe-Romo, F. J.; Chae, H. K.; O’Keeffe, M.; Yaghi, O. M. Exceptional Chemical and Thermal Stability of Zeolitic Imidazolate Frameworks. *Proc. Natl. Acad. Sci. U. S. A.* **2006**, *103*, 10186–10191.
- (61) Lock, N.; Wu, Y.; Christensen, M.; Cameron, L. J.; Peterson, V. K.; Bridgeman, A. J.; Kepert, C. J.; Iversen, B. B. Elucidating Negative Thermal Expansion in MOF-5. *J. Phys. Chem. C* **2010**, *114*, 16181–16186.
- (62) Tsoufis, T.; Tampaxis, C.; Spanopoulos, I.; Steriotis, T.; Katsaros, F.; Charalambopoulou, G.; Trikalitis, P. N. High-Quality Graphene Sheets Decorated with ZIF-8 Nanocrystals. *Microporous Mesoporous Mater.* **2018**, *262*, 68–76.
- (63) Fairen-Jimenez, D.; Moggach, S. A.; Wharmby, M. T.; Wright, P. A.; Parsons, S.; Düren, T. Opening the Gate: Framework Flexibility in ZIF-8 Explored by Experiments and Simulations. *J. Am. Chem. Soc.* **2011**, *133*, 8900–8902.
- (64) Thommes, M.; Kaneko, K.; Neimark, A. V.; Olivier, J. P.; Rodriguez-Reinoso, F.; Rouquerol, J.; Sing, K. S. Physisorption of Gases, with Special Reference to the Evaluation of Surface Area and Pore Size Distribution (IUPAC Technical Report). *Pure Appl. Chem.* **2015**, *87*, 1051–1069.
- (65) Gómez-Gualdrón, D. A.; Moghadam, P. Z.; Hupp, J. T.; Farha, O. K.; Snurr, R. Q. Application of Consistency Criteria to Calculate BET Areas of Micro- and Mesoporous Metal-Organic Frameworks. *J. Am. Chem. Soc.* **2016**, *138*, 215–224.
- (66) Wang, T. C.; Bury, W.; Gómez-Gualdrón, D. A.; Vermeulen, N. A.; Mondloch, J. E.; Deria, P.; Zhang, K.; Moghadam, P. Z.; Sarjeant, A. A.; Snurr, R. Q.; Stoddart, J. F.; Hupp, J. T.; Farha, O. K. Ultrahigh Surface Area Zirconium MOFs and Insights into the Applicability of the BET Theory. *J. Am. Chem. Soc.* **2015**, *137*, 3585–3591.
- (67) Tanaka, H.; Ohsaki, S.; Hiraide, S.; Yamamoto, D.; Watanabe, S.; Miyahara, M. T. Adsorption-Induced Structural Transition of ZIF-8: A Combined Experimental and Simulation Study. *J. Phys. Chem. C* **2014**, *118*, 8445–8454.
- (68) Cravillon, J.; Münzer, S.; Lohmeier, S.-J.; Feldhoff, A.; Huber, K.; Wiebcke, M. Rapid Room-Temperature Synthesis and Characterization of Nanocrystals of a Prototypical Zeolitic Imidazolate Framework. *Chem. Mater.* **2009**, *21*, 1410–1412.
- (69) Ordoñez, M. J. C.; Balkus, K. J.; Ferraris, J. P.; Musselman, I. H. Molecular Sieving realized with ZIF-8/Matrimid® Mixed-Matrix Membranes. *J. Membr. Sci.* **2010**, *361*, 28–37.
- (70) Luo, Z.; Chaemchuen, S.; Zhou, K.; Verpoort, F. Ring-Opening Polymerization of L-Lactide to Cyclic Poly(Lactide) by Zeolitic Imidazole Framework ZIF-8 Catalyst. *ChemSusChem* **2017**, *10*, 4135–4139.
- (71) Mousavi, B.; Luo, Z.; Phatanasri, S.; Su, W.; Wang, T.; Chaemchuen, S.; Verpoort, F. One-Step Synthesis of 2,5-Bis-(chloromethyl)-1,4-dioxane from Epichlorohydrin Using ZIF-8, Taking Advantage of Structural Defects. *Eur. J. Inorg. Chem.* **2017**, *2017*, 4947–4954.
- (72) Nordin, N. A. H. M.; Ismail, A. F.; Mustafa, A.; Goh, P. S.; Rana, D.; Matsuura, T. Aqueous Room Temperature Synthesis of Zeolitic Imidazole Framework 8 (ZIF-8) with Various Concentrations of Triethylamine. *RSC Adv.* **2014**, *4*, 33292–33300.
- (73) Sabo, M.; Henschel, A.; Fröde, H.; Klemm, E.; Kaskel, S. Solution Infiltration of Palladium into MOF-5: Synthesis, Physisorption and Catalytic Properties. *J. Mater. Chem.* **2007**, *17*, 3827.
- (74) Liu, D.; Purewal, J. J.; Yang, J.; Sudik, A.; Maurer, S.; Mueller, U.; Ni, J.; Siegel, D. J. MOF-5 Composites Exhibiting improved Thermal Conductivity. *Int. J. Hydrogen Energy* **2012**, *37*, 6109–6117.
- (75) Britt, D.; Tranchemontagne, D.; Yaghi, O. M. Metal-Organic Frameworks with High Capacity and Selectivity for Harmful Gases. *Proc. Natl. Acad. Sci. U. S. A.* **2008**, *105*, 11623–11627.
- (76) Pauchard, M.; Huber, S.; Méallet-Renault, R.; Maas, H.; Pansu, R.; Calzaferri, G. Time- and Space-Resolved Luminescence of Photonic Dye-Zeolite Antenna. *Angew. Chem., Int. Ed.* **2001**, *40* (15), 2839–2842.
- (77) Zhang, Z.; Wei, Z.; Meng, F.; Su, J.; Chen, D.; Guo, Z.; Xing, H. RhB-Embedded Zirconium-Naphthalene Based Metal-Organic Framework Composite as Luminescent Self-Calibrating Platform for Selective Detection of Inorganic Ions. *Chem. - Eur. J.* **2020**, *26*, 1661.